J Adv Ceram

Research Article

Atomic-scale elucidation of attenuation mechanisms underlying exceptional electromagnetic wave absorption of SiZrBCN ceramic nanocomposites

Zhongqi Wang[1], Shuibin Wang[1], Han Fei[1], Tianxing Jiang[1], Bo Feng[2], Qingbo Wen[1,✉], Xiang Xiong[1]

Cite this article: Wang Z, Wang S, Fei H, et al. *J Adv Ceram* 2026, **15**(1): 9221221. https://doi.org/10.26599/JAC.2025.9221221

ABSTRACT: To elucidate the atomic-scale mechanisms governing electromagnetic wave (EMW) attenuation in polymer-derived ceramics, a SiZrBCN ceramic nanocomposite was prepared via chemical modification of polyborosilazane with tetrakis(dimethylamino) zirconium(IV), followed by pyrolysis and annealing. Advanced characterization methods combined with first-principles calculations via density functional theory (DFT) were employed to investigate the structural evolution, dielectric properties, and attenuation mechanisms of the nanocomposites. The results show that after pyrolysis at $T \leq$ 1400 °C, the SiZrBCN is in an amorphous state. As the annealing temperature increases, ZrC_xN_{1-x}, SiC, and β-Si_3N_4 initially precipitate at 1500 °C. When the temperature increases to 1800 °C, ZrC_xN_{1-x} transforms into ZrB_2, forming SiC/ZrB_2 multiphase ceramic nanocomposites. With the incorporation of Zr, SiZrBCN-16, after annealing at 1600 °C, exhibits excellent EMW absorption performance, achieving a maximum effective absorption bandwidth of 6.03 GHz (thickness: 1.65 mm) and a minimum reflection loss of −44.1 dB (thickness: 1.9 mm). In addition to the conductive loss caused by the free carbon network, DFT analysis revealed two primary dielectric loss mechanisms that result in exceptional absorbing performance: (1) Electronegativity-driven charge separation in ZrC_xN_{1-x} solid solutions facilitates the formation of electric dipoles; (2) interfacial lattice distortion and atomic disparity across the interface at the ZrC(001)/β-Si_3N_4(001) and ZrN(100)/SiC(110) boundaries induce electronic reconstruction and charge separation.

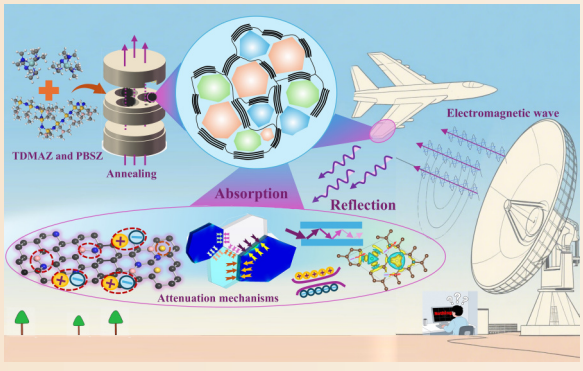

KEYWORDS: polymer-derived ceramics; polarization loss; microstructure; electromagnetic wave absorption; density functional theory

1 Introduction

SiBCN ceramics, as among the most widely used polymer-derived ceramics, have been extensively investigated owing to their advantages, including excellent high-temperature stability and oxidation resistance, and electromagnetic wave (EMW) absorption is considered one of their most promising applications [1–3]. Generally, SiBCN-based ceramics are derived from polyborosilazane (PBSZ) at elevated temperatures [4]. However, unmodified SiBCN ceramics exhibit inferior EMW absorption performance due to the absence of electromagnetic loss phases [5]. To enhance their EMW attenuation capability, the primary approach involves either chemical structural design or direct incorporation of secondary phases to generate electromagnetic loss components [6–10]. For instance, Ding *et al.* [11] prepared SiBCN fibers by electrospinning, leveraging turbostratic carbon and nano-SiC grains to enhance conductive loss and interfacial polarization, thereby achieving an effective absorption bandwidth (EAB) of 5.2 GHz. Song *et al.* [12] prepared SiBCNHf, a nanostructure comprising *in situ*-formed HfC, SiC, and HfB_2, which developed during the annealing process. The coexistence of multiple phases induced significant polarization loss, resulting in a minimum reflection loss of −50 dB, and the antioxidant performance was improved. Therefore, SiBCN is considered a great potential material for EMW absorption.

The dissipation of electromagnetic wave energy in multiphase ceramics is governed primarily by mechanisms including interfacial polarization, dipole polarization, defect-induced polarization, and conductive loss. The electromagnetic wave absorption performance can be enhanced by tailoring the microstructure to achieve a synergistic enhancement via multiple mechanisms, such as SiZrCN [13,14], SiC/HfC_xN_{1-x}/C [15], SiBCN/Al_2O_3 [16], and SiBCN–ZrO_2/ZrC/ZrB_2/SiC [7]. Hence, interface engineering is considered a primary strategy for

[1] State Key Laboratory of Powder Metallurgy, Central South University, Changsha 410083, China. [2] Air Force Engineering University, Xi'an 710051, China.

✉ Corresponding author. E-mail: wentsingbo@csu.edu.cn

Received: September 8, 2025; Revised: November 20, 2025; Accepted: November 25, 2025

enhancing the electromagnetic wave absorption performance of SiBCN-based ceramics. Yang *et al.* [17] incorporated samarium (Sm) as a catalyst into SiBCN to modulate crystallinity while promoting defect generation, attaining an EAB of 6.87 GHz. Zhao *et al.* [18] introduced SiBCN into a porous Si_3N_4 substrate to enhance interfacial polarization by constructing interfaces between nanocrystalline and amorphous phases within the SiBCN material. Zhang *et al.* [19] fabricated a three-dimensional (3D) structure by annealing a mixture of graphene and SiBCN, which established B–C–N covalent bonds at the interface between the ceramic matrix and graphene. This structure achieved an effective absorption bandwidth covering the entire X-band at a matching thickness of 3 mm. Luo *et al.* [20] synthesized cobalt-containing silicon boron carbonitride (derived from MOFs, denoted as MOF/SiBCN) nanomaterials. Increasing the content of dielectric phases such as SiC and CoSi increased the dielectric loss and improved the impedance matching of the material. Extensive research has established a strong correlation between electromagnetic wave absorption performance and its underlying mechanisms [21]. However, the electromagnetic loss mechanisms within multiphase ceramics remain inadequately elucidated. A significant knowledge gap persists, particularly in the analysis of loss behaviors at heterogeneous interfaces. Furthermore, existing theoretical frameworks lack the explanatory power to fully describe the cross-scale and multi-physical field coupling processes involved. This limitation fundamentally constrains the rational design of compositions and the strategic modulation of properties in multiphase ceramics based on the optimization of dielectric loss mechanisms.

In addition, research has focused primarily on characterizing structural evolution and phase composition [22–25], but dielectric loss mechanisms are generally attributed to interfacial polarization from abundant interfacial structures and relaxation phenomena of electric dipoles within the material under alternating electromagnetic fields; such polarization behavior can be modeled via Debye theory [14,26,27]. In practical scenarios, the origins of interfacial polarization may be more complex, particularly as grain formation and growth during annealing processes result in sophisticated microstructures [28,29]. The physical properties of interfaces exhibit distinct energy states depending on variations in atomic species, concentration, and structural configurations [30]. This manifests as significant modifications in band structures and electron redistribution, where spatial charge density variations generate new electronic orbital energy levels [31]. Notably, charge redistribution at heterogeneous interfaces induces separation of positive and negative charge centers, profoundly influencing the material's electromagnetic response characteristics [32]. Consequently, to elucidate microstructure–macroscopic property relationships, researchers increasingly employ theoretical computations as tools to decipher intergranular physical phenomena [33–35]. The construction of crystalline models to analyze charge transfer and bonding characteristics provides critical insights into the atomic-scale origins of interfacial polarization. Given the abundance of interfaces in polymer-derived nanoceramics, establishing atomistic models and probing electronic structures are essential for guiding experimental design.

Therefore, to investigate the microscopic mechanisms of EMW absorption in SiBCN-based composite ceramics, we incorporated zirconium-containing metal amides into PBSZ. Subsequent high-temperature annealing yielded nanocomposite ceramic powders. To minimize energy and time consumption, we designed a graphite mold compatible with spark plasma sintering (SPS) technology. This system enables non-pressure high-temperature annealing of ceramic powders by leveraging the rapid heating capabilities of SPS equipment, thereby significantly reducing the annealing duration. The influence of the annealing temperature on phase transformations was systematically examined. Leveraging the phase characterization results, we constructed relevant crystal structures within the ceramics and established potential interfacial models between the crystalline phases. Density functional theory (DFT) calculations were then performed to analyze the electronic structures in both the crystalline and interfacial regions, providing atomistic-scale physical insights to elucidate the origin of interfacial polarization at the electronic level.

2 Experimental

The SiZrBCN precursors were obtained by the reaction of 90 wt% PBSZ and 10 wt% metal amides, named tetrakis (dimethylamino) zirconium(IV) (TDMAZ) (Nanjing Ai Mou Yuan Scientific equipment Co., Ltd., China). The specific synthesis route is as follows: In an inert atmosphere, TDMAZ and PBSZ are dissolved in xylene, mixed through a titration process, and stirred at 70 °C until the reaction is complete to obtain the Zr-PBSZ precursor. The Zr-PBSZ precursor and SiBCN were pyrolyzed at 1100 °C for 2 h in a N_2 atmosphere. Furthermore, pyrolyzed powder can be charged into isostatic graphite suitable for plasma sintering (SPS) equipment, which has a central hole structure that can be applied for high-vacuum and high-current heating. These samples subsequently underwent non-pressure heat treatment at 1300, 1400, 1500, 1600, and 1800 °C under high vacuum (P < 10 Pa), employing rapid heating rates (100 °C/min) with 20 min dwell time at peak temperatures. The specific fabrication process is shown in Fig. 1.

Furthermore, to investigate the relationships among the dielectric properties, electromagnetic wave absorption capabilities, and internal interfacial/electronic structures of multiphase ceramics, we constructed bulk ceramic and interfacial crystal models. These subsequently underwent geometry optimization and electronic structure calculations. First-principles calculations based on DFT were performed via the Cambridge sequential total energy package (CASTEP). The exchange–correlation functional employed the Perdew–Burke–Ernzerhof (PBE) variant within the generalized gradient approximation (GGA) framework. A plane-wave basis set cutoff of 500 eV was applied. Structural optimization utilized the Troullier–Martins pseudopotential with soft densities (LBFGS) algorithm with convergence thresholds of 1×10^{-5} eV/atom for total energy, 0.03 eV/Å for maximum force, 0.01 Å for maximum displacement, and 0.05 GPa for maximum stress. The lattice parameters and atomic positions were fully relaxed until all the convergence criteria were satisfied.

The crystallographic properties and chemical compositions of SiZrBCN ceramics subjected to different heat treatments were comprehensively characterized via X-ray diffraction (XRD), Raman spectroscopy, and X-ray photoelectron spectroscopy (XPS) analyses. The XRD patterns were recorded via a powder diffractometer (D8 Advance, Bruker, Germany) with a Cu Kα1 radiation source (λ = 1.541874 Å). Raman spectroscopy was conducted on a micro-Raman spectrometer (DXR3, Thermo Fisher Scientific, USA) with an argon laser (wavelength of 532 nm) from 500 to 3500 cm^{-1}. An X-ray photoelectron spectrometer (ESCALAB 250Xi, Thermo Fisher Co., USA) was used to characterize the atomic bonding state with an Al Kα radiation source in constant analyzer energy (CAE) mode (20.0 eV) with an energy step of 0.05 eV. A transmission electron microscope (TEM; Talos, F200X, The Czech Republic) equipped with an energy-

dispersive X-ray spectrometer (EDS) was used to characterize the microstructures of the ceramics.

3 Results and discussion

3.1 Phase and microstructure analysis of Si(Zr)BCN ceramics

XRD patterns reveal the structural evolution of the SiBCN and SiZrBCN ceramics at different annealing temperatures (Fig. 2(a)). Both SiBCN and SiZrBCN maintained an amorphous structure at 1400 °C. At 1500 °C, the diffraction peaks of SiBCN corresponded to β-SiC and α-SiC, and the observed crystallization temperature was lower than those reported in previous studies, which is attributed to the high vacuum heating environment [36]. Moreover, SiZrBCN-15 (annealed at 1500 °C) exhibited diffraction peaks corresponding to ZrC_xN_{1-x}, SiC (mainly β-SiC), and β-Si_3N_4 crystalline phases. Upon increasing the temperature to 1600 °C, the increased peak intensities for both ceramics indicated an improvement in crystallinity. At 1800 °C, the characteristic peaks of α-SiC in SiBCN disappeared, leaving only the β-SiC phase. Notably, the phase composition of SiZrBCN-18 (annealed at 1800 °C) transitioned to ZrB_2 and SiC, where β-Si_3N_4 was completely consumed through a reaction with carbon to form additional SiC [12]. As shown in Fig. 2, the diffraction peaks observed at 2θ values of approximately 25.2°, 32.6°, 41.6°, 51.7°, and 58.1° can be exclusively indexed to the (001), (100), (101), (002), and (110) lattice planes of crystalline ZrB_2, respectively. The presence of these distinct peaks signifies the formation of a well-defined crystalline ZrB_2 structure. Furthermore, the distinct differences in the Zr-containing phases observed between the 1600 and 1800 °C annealing temperatures, which directly correlate with the chemical state of boron, call for further characterization to elucidate the underlying complex transitions.

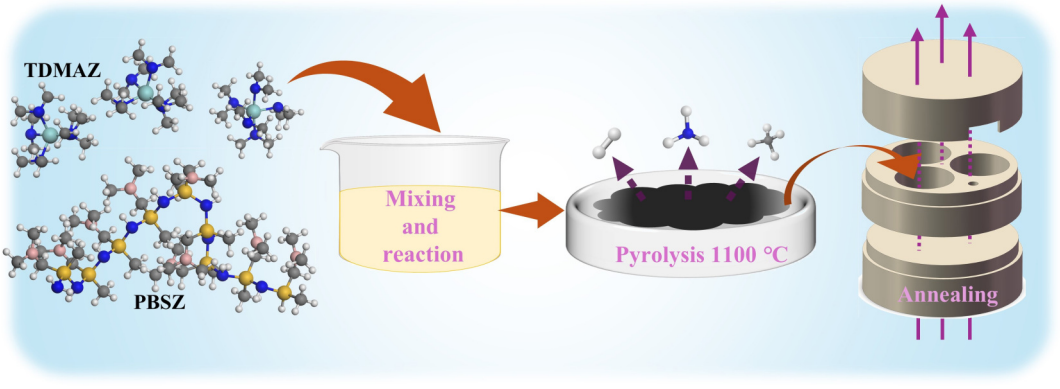

Fig. 1 Schematic diagram for preparation of SiZrBCN ceramics, including synthesis route, pyrolysis, and high-temperature annealing.

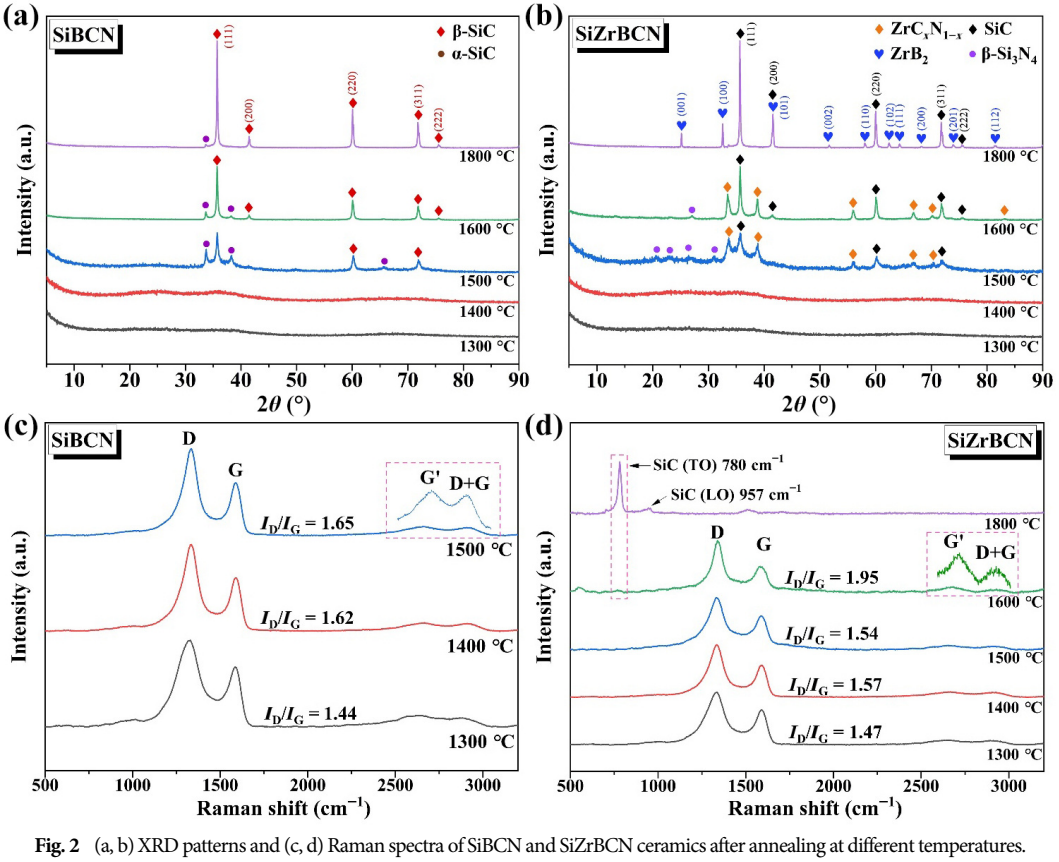

Fig. 2 (a, b) XRD patterns and (c, d) Raman spectra of SiBCN and SiZrBCN ceramics after annealing at different temperatures.

The Raman spectra of the SiBCN and SiZrBCN ceramics annealed at different temperatures revealed the process of ordering transformation of free carbon in the matrix, as shown in Figs. 2(c) and 2(d). All the samples exhibit two prominent peaks at approximately 1335 and 1588 cm^{-1}, which are attributed to the D and G bands of carbon, respectively. In general, the D-band corresponds to disordered sp^3-hybridized carbon, whereas the G-band originates from in-plane stretching vibrations of sp^3-bonded carbon atoms. In addition, G′ and D+G bands can be observed at 2681 and 2929 cm^{-1}, with the former reflecting the second-order Raman scattering peak associated with sp^2-hybridized carbon materials, arising from the double-resonance scattering process, and the latter resulting from the sum of the frequencies of the D peak and G peak. The I_D/I_G values of the SiBCN and SiZrBCN ceramics gradually increase with increasing temperature, whereas the degree of overlap between the D peak and G peak decreases progressively. This is because free carbon gradually migrates and aggregates to form carbon domains during the annealing process. Increasing the annealing temperature leads to gradual growth and more sufficient aggregation of these carbon domains; however, the rapid heating conditions restrict the ordering process of the carbon domains. Among them, the density of defects caused by vacancies and heteroatoms such as Si/B/N increases, which weakens their ordered characteristics. Moreover, the types of defects in the carbon domains gradually decrease with increasing temperature, resulting in reduced dispersion of the vibration frequencies of the D and G peaks, which in turn manifests as less overlap and sharper peaks. However, the samples of SiBCN-16 and SiBCN-18 failed to detect valid characteristic peaks because of fluorescence interference. For the SiZrBCN-16 ceramic, an I_D/I_G value of 1.94 indicates significant carbon disorder, which in turn points to more defects within the multiphase coexisting structure. In addition, there are two bands centered at 781 and 955 cm^{-1} for SiZrBCN-18, which are assigned to the transversal optic (TO) mode and the longitudinal optical (LO) phonon mode of SiC, respectively [12,37]; these bands directly correspond to extensive carbon consumption during SiC formation and align with XRD observations for the SiZrBCN-18 sample.

Moreover, during the annealing process, free carbon and ordered carbon collectively form a continuous three-dimensional network architecture across ceramic particle surfaces and grain boundaries, and boron and nitrogen atoms ubiquitously occupy carbon sites within this network, collectively constituting complicated B–C–N networks [38,39]. Therefore, the formation of the ZrB_2 phase in SiZrBCN-18 is closely related to the B–C–N networks. To further elucidate the chemical states of the constituent elements, XPS measurements of the SiZrBCN ceramic are presented in Fig. 3. The survey spectrum of SiZrBCN-16 in Fig. 3(a) confirms the characteristic peaks corresponding to the Si 2p, B 1s, C 1s, N 1s, and Zr 3d orbitals [40]. The peak deconvolution results exhibit excellent consistency with the XRD analyses. Notably, spectral deconvolution of B, C, and N reveals pairwise chemical bonding between these elements, strongly supporting the formation of three-dimensional B–C–N networks [41]. In addition, these well-connected carbon-dominated networks exhibit exceptional continuity and electrical conductivity. Under applied electromagnetic (EM) fields, these networks provide continuous pathways for directional electron migration while minimizing electron scattering at grain boundaries. This mechanism of electromagnetic wave energy dissipation via electron movement is termed conductive loss [42,43].

On the basis of the above analysis, we propose a temperature-dependent phase evolution mechanism for SiZrBCN ceramics: Annealing at 1500 °C, ZrC_xN_{1-x}, SiC, and β-Si_3N_4 grains initially nucleate, whereas boron predominantly resides within three-dimensional B–C–N networks at grain boundaries and particle surfaces. At 1600 °C, the phase configuration retains structural stability throughout the isothermal hold period, whereas the crystallinity progressively increases. Upon further heating to 1800 °C, the carbon consumption through the reaction with β-Si_3N_4 progressively disintegrates the B–C–N networks. Liberated nitrogen evolves as N_2 gas, whereas boron atoms incorporate into the ZrC_xN_{1-x} lattice by substituting carbon and nitrogen sites, ultimately forming ZrB_2 [39]. Potential reaction pathways during this process are illustrated in Reactions (1)–(3).

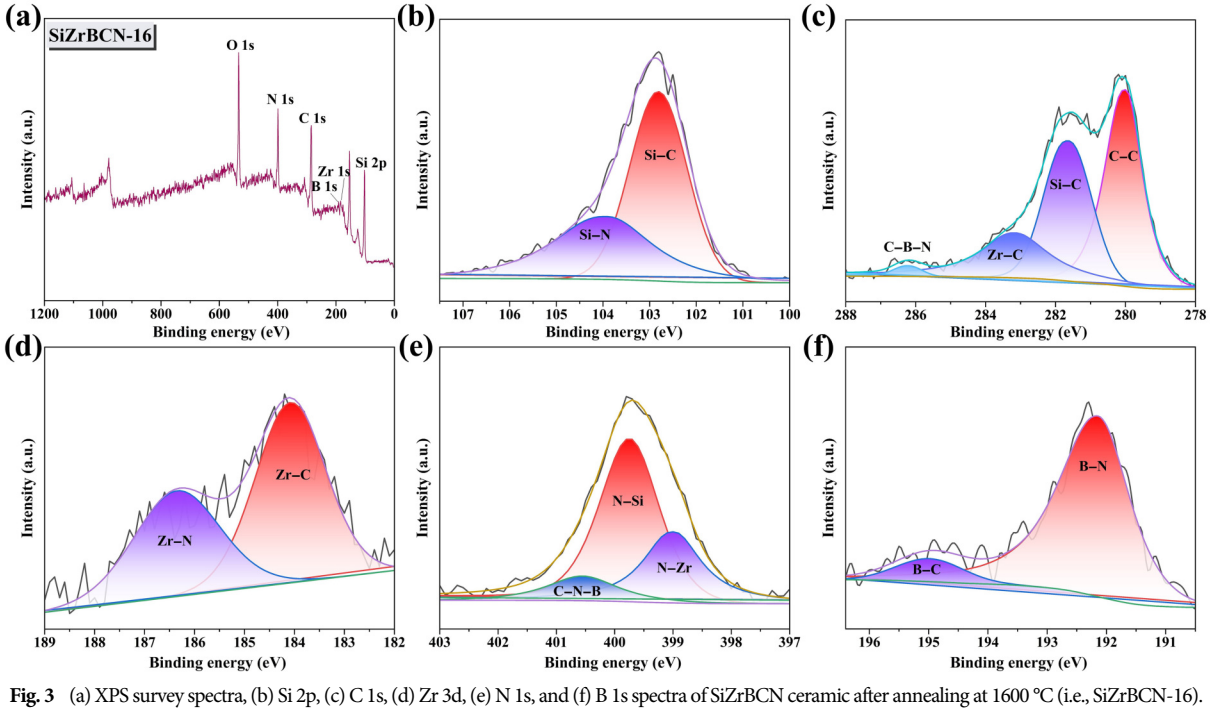

Fig. 3 (a) XPS survey spectra, (b) Si 2p, (c) C 1s, (d) Zr 3d, (e) N 1s, and (f) B 1s spectra of SiZrBCN ceramic after annealing at 1600 °C (i.e., SiZrBCN-16).

$$ZrC + 2BCN + Si_3N_4 = ZrB_2 + 3SiC + 3N_2(g)\uparrow \quad (1)$$

$$ZrC + 2BCN = ZrB_2 + 3C + N_2(g)\uparrow \quad (2)$$

$$2ZrN + 4BCN = 2ZrB_2 + 4C + 3N_2(g)\uparrow \quad (3)$$

For simplification, the initial phases are represented as ZrC, ZrN, and BCN in the reaction schemes. The calculated Gibbs free energy values ($\Delta G = \Delta G_{products} - \Delta G_{reactants}$) indicate that both reactions are thermodynamically favorable [44]. Furthermore, under high-vacuum conditions during isothermal processing, the reduced N_2 partial pressure shifts the reaction equilibrium forward, whereas transient thermal gradients collectively drive these transformations. Consequently, incorporating metal amides into PBSZ precursors demonstrates potential for synthesizing novel TMB_x/SiC ceramic composites via this method.

TEM was further employed to examine the detailed microstructure of the SiZrBCN ceramics annealed at 1600 and 1800 °C. Figure 4(a) shows the well-crystallized morphologies of both the ZrC_xN_{1-x} and SiC grains. The elemental mapping images in Fig. 4(e) reveal that Si, B, C, and N are distributed throughout the particles, with no apparent regions of absence in their distribution, albeit with incomplete uniformity. This observation confirms that the matrix possesses an actual composition of SiBCN but is primarily SiC, which is consistent with the XRD results. Zr and N are predominantly located within the ZrC_xN_{1-x} crystals, which are uniformly dispersed throughout the SiC matrix, with a small amount of β-Si_3N_4 (hardly detectable in the TEM images). Interestingly, B, to some extent, is enriched around the ZrC_xN_{1-x} crystals, which indicates that a few ZrB_2 clusters may form at 1600 °C even though they cannot be detected by XRD. Finer microstructural details at the interfaces between ZrC_xN_{1-x} and SiC can be observed from the high-resolution TEM (HRTEM) images presented in Figs. 4(b) and 4(c). Lattice fringes are observed to distort at the intergranular interfaces. The crystal surfaces are covered by amorphous carbon shells. Moreover, abundant interfacial structures are ubiquitously observed between distinct nanograins within the ceramic matrix. The differences in the crystal structure and lattice parameters across these interfaces generate lattice mismatches, which induce a high density of defects. These defects constitute abundant electric polarization centers [45,46]. Moreover, compositional variations induce charge accumulation at semicoherent interfaces, thereby modulating the interfacial polarization behavior [42]. In addition, ordered carbon ribbons are present on the particle surfaces, as shown in

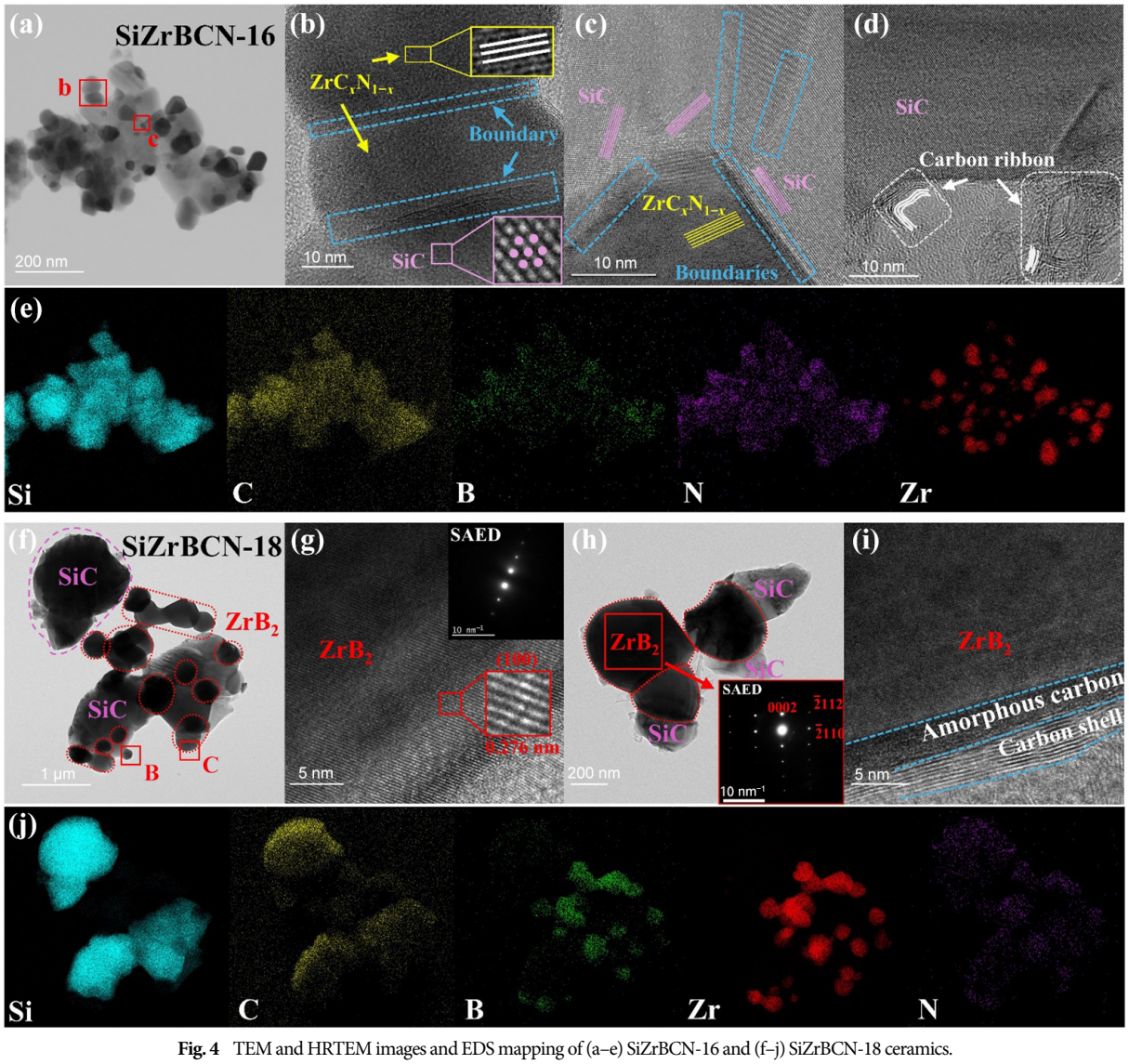

Fig. 4 TEM and HRTEM images and EDS mapping of (a–e) SiZrBCN-16 and (f–j) SiZrBCN-18 ceramics.

清華大学出版社 Tsinghua University Press | SciOpen

Fig. 4(d). These interconnected ribbons, which adhere to the grain surfaces, form the foundation of a three-dimensional carbon network. Therefore, the presence of these features, which are conducive to both polarization loss and conductive loss, endows the SiZrBCN-16 ceramic with excellent electromagnetic wave absorption properties.

The TEM images of the SiZrBCN-18 ceramic (Fig. 4(f)) reveal larger grain sizes, corresponding to an increased degree of crystallinity annealed at 1800 °C. The HRTEM image (Fig. 4(g)) shows distinct lattice fringes of ZrB_2, and the corresponding selected-area electron diffraction (SAED) pattern confirms that these fringes can be indexed to the (100) crystallographic plane. Figure 4(h) displays another ZrB_2 grain. The SAED pattern demonstrates its single-crystalline nature. Notably, a ZrB_2/amorphous carbon/carbon shell multilayered structure can be observed in Fig. 4(i). When the temperature increases to the point where ZrB_2 begins to form, the carbon ribbons near the ceramic grains are disrupted, releasing B, C, and N atoms. The B atoms are incorporated into the ZrC_xN_{1-x} crystal lattice, accompanied by the precipitation of C and N atoms (with N atoms forming N_2). The carbon atoms released during these two transformation processes accumulate between the surface of the ZrB_2 grains and the external ordered carbon structure. The outward expansion of the ZrB_2 grains leads to an increase in the carbon content accumulated on the surface and a further reduction in the diffusion space for the carbon atoms. Consequently, under short-term heating conditions, an amorphous carbon intermediate layer forms. The external carbon ribbons bond with surface defects or dangling bonds of amorphous carbon and undergo further ordering through high-temperature treatment, ultimately resulting in this unique multilayer structure. Figure 4(j) reveals a pronounced elemental segregation within the SiZrBCN-18 ceramic particles. This elemental mapping further elucidates the phase evolution under high-temperature annealing conditions. Notably, the B signal is more concentrated than that in SiZrBCN-16, providing further evidence for the release of B atoms from the original B–C–N network and their subsequent incorporation into the ZrB_2 lattice during annealing at 1800 °C.

3.2 Dielectric and EMW absorption properties of Si(Zr)BCN ceramics

The electromagnetic wave response of SiBCN and SiZrBCN ceramics annealed at various temperatures was characterized via a vector network analyzer (VNA). The samples were fabricated into coaxial rings with an outer diameter of 7.00 mm and an inner diameter of 3.04 mm, and the mass ratio of powder to paraffin was 3 : 2. The electromagnetic parameters were measured via the coaxial method over the 1–18 GHz frequency range. The real part of the complex permittivity (ε') represents the storage capacity, which correlates directly with the polarization intensity, whereas the imaginary part of the complex permittivity (ε'') reflects the conversion efficiency of electromagnetic energy to thermal energy, with its magnitude arising collectively from relaxation, conduction, and polarization losses [10].

Notably, the ε' and ε'' values for both the SiBCN and SiZrBCN ceramics tend to increase as the annealing temperature increases (Figs. 5(a) and 5(b)). For example, the real part of the relative permittivity of SiBCN ceramics increases from 6.2–6.4 (for SiBCN-13) to 12.7–24.3 (for SiBCN-16), whereas that of SiZrBCN ceramics increases from 5.9–6.1 (for SiZrBCN-13) to 8.5–14.7 (for SiZrBCN-16). This is because, as the temperature increases, the content of lossy phases inside the ceramics gradually increases, and the coexistence of multiple electromagnetic wave absorption mechanisms further enhances the ceramic response capability to electromagnetic waves. With increasing frequency,

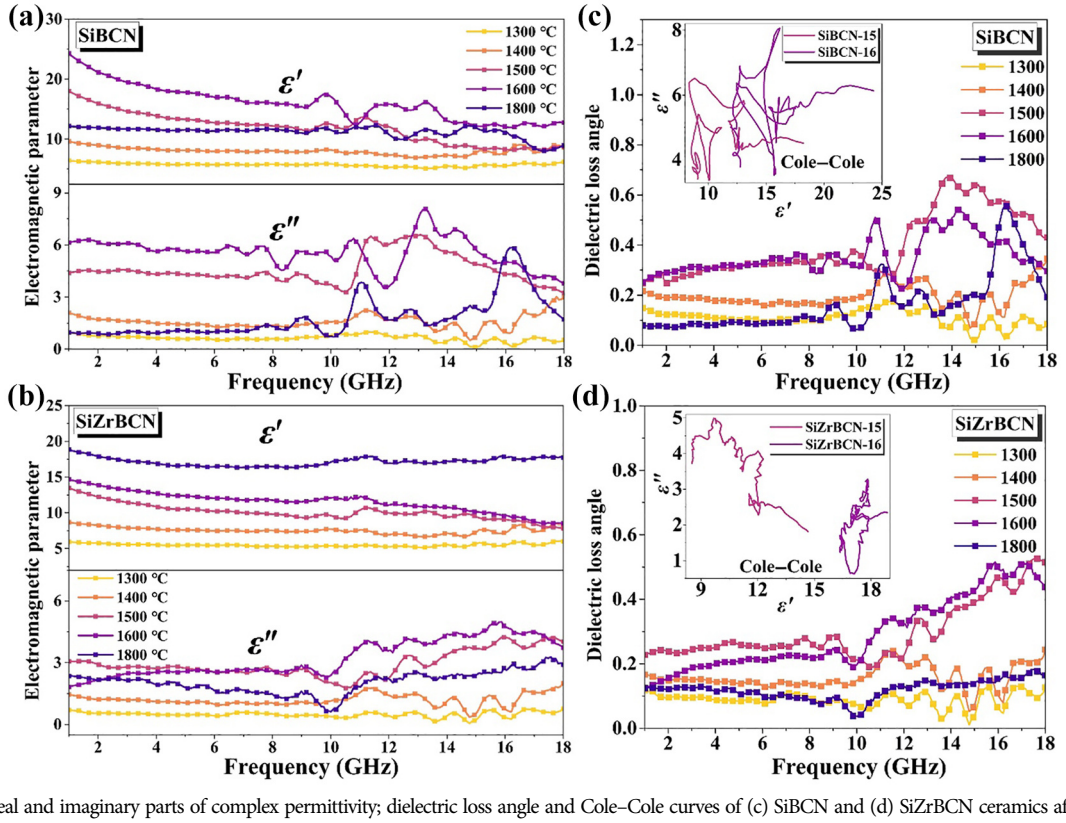

Fig. 5 (a, b) Real and imaginary parts of complex permittivity; dielectric loss angle and Cole–Cole curves of (c) SiBCN and (d) SiZrBCN ceramics after annealing at 1300, 1400, 1500, 1600, and 1800 °C, respectively.

both ceramics exhibit a decreasing trend in the real part of the relative permittivity and an increasing trend in the imaginary part. This is because polarization relaxation loss dominates both the SiBCN and SiZrBCN ceramics [47]. The polarization processes induced by interface polarization, electric dipoles, and other factors gradually fail to keep up with the variation rhythm of the alternating electric field as the electromagnetic wave frequency increases, resulting in a significant lag, which weakens the polarization response capability of the materials. Moreover, the dipole relaxation lag gives rise to notable energy dissipation, leading to an increase in dielectric loss, which corresponds to an increase in the imaginary part of the dielectric constant. Moreover, SiBCN-18 retains only the SiC ceramic phase, leading to an insufficient response capability to electromagnetic waves and thus a sudden decrease in the real and imaginary parts of the dielectric constant. For the SiZrBCN-18 ceramics, the imaginary part also decreases compared with that of the SiZrBCN-16 ceramics. Although the interface polarization mechanism between the ZrB_2 and SiC phases enables them to retain a certain degree of electromagnetic loss capability, the relatively high real part makes it difficult for electromagnetic waves to penetrate the interior of the material, and the destruction of the three-dimensional conductive network reduces conductive loss. As presented in Figs. 5(c) and 5(d), only the dielectric loss tangents of SiBCN-15, SiBCN-16, SiZrBCN-15, and SiZrBCN-16 reach above 0.5 within the 10–18 GHz frequency band. This high value of the loss tangent is critical, as it signifies that the electromagnetic energy dissipation capacity of these materials is sufficiently strong, which is a fundamental prerequisite for achieving effective EMW absorption [41]. Among these samples, the Cole–Cole plots indicate that the ceramics exhibit multiple relaxation processes under the action of electromagnetic waves, which implies excellent electromagnetic wave absorption performance [48].

On the basis of transmission line theory, the reflection loss (RL) and impedance matching were calculated via Eqs. (4) and (5) for SiBCN-15, SiBCN-16, SiZrBCN-15, and SiZrBCN-16 at various thicknesses [49,50].

$$\mathrm{RL} = 20\log|(Z_{\mathrm{in}} - Z_0)/(Z_{\mathrm{in}} + Z_0)| \tag{4}$$

$$Z_{\mathrm{in}}/Z_0 = \sqrt{\frac{\mu_{\mathrm{r}}}{\varepsilon_{\mathrm{r}}}}\tanh\left(\mathrm{j}\frac{2\pi fd}{c}\sqrt{\mu_{\mathrm{r}}\varepsilon_{\mathrm{r}}}\right) \tag{5}$$

Figures 6(a) and 6(d) show that SiBCN-15, SiBCN-16, SiZrBCN-15, and SiZrBCN-16 exhibit good impedance matching degrees at thicknesses of 1.6–1.7 mm. This means that electromagnetic waves can fully penetrate the interior of materials and dissipate energy through multiple reflections. In addition, owing to differences in annealing temperature, the distinct phase formations in Si(Zr)BCN ceramics result in varied microstructures, which in turn lead to noticeable differences in EMW absorption performance. For example, SiBCN-15 achieves a maximum effective absorption bandwidth (EAB_{max}) of 5.18 GHz at 1.75 mm (Fig. 6(b)), whereas SiBCN-16 exhibits an EAB_{max} of only 3.74 GHz at 1.6 mm (Fig. 6(c)). This can be attributed to the preserved carbon network and the coexistence of two SiC polymorphs in SiBCN-15, which creates a multilevel interfacial structure. This promotes synergistic enhancement of interfacial polarization and conductive loss, leading to broadband absorption. Moreover, its RL_{min} reaches −50.1 dB at 1.7 mm, indicating that approximately 99.999% of the incident EMW energy at 14.2 GHz can be absorbed. In contrast, SiBCN-16 predominantly retains only β-SiC, and the disruption of the carbon network simplifies the loss mechanism, resulting in a narrow absorption bandwidth (3.74 GHz at 1.6 mm) and a weaker reflection loss (−46.2 dB at 2.35 mm). For SiZrBCN-15 ceramics, the introduction of Zr enhances the thermal stability of the ceramic matrix. However, the relatively low degree of crystallization implies limited precipitation of loss–active phases and thus a weaker EMW absorption capability. Consequently, it shows only −17.9 dB RL_{min} (at 1.65 mm) and a narrower absorption bandwidth than that of SiBCN-15 (Fig. 6(e)). However, after annealing at 1600 °C, the SiZrBCN-16 ceramic exhibits a multiphase structure composed of β-Si_3N_4, SiC, ZrC_xN_{1-x}, and carbon. The increased interface density effectively enhances the interfacial polarization. The Raman and TEM results confirm the stability of the carbon network, preserving the conduction loss mechanism. Furthermore, the charge separation caused by electronegativity differences within the ZrC_xN_{1-x} solid solution generates electric dipoles, which further strengthen dipole relaxation loss (this will be systematically discussed in subsequent computational results). Under the combined effects of conductive loss, polarization loss, and dipole polarization, the EMW dissipation capability is significantly improved, achieving an EAB of 6.03 GHz at 1.65 mm. Moreover, the RL_{min} reaches −44.1 dB at 1.9 mm (Fig. 6(f)), which is nearly 2.5 times greater than that of SiZrBCN-15. Furthermore, to investigate the stealth performance of SiZrBCN-16 ceramics, radar scattering cross-section (RCS) values were evaluated [51]. The coating thickness was set to 1.9 mm, and the original perfect electrical conductor (PEC) thickness was 1 mm. The model and the scattered signal intensity are shown in Figs. 6(g) and 6(h). The 3D scattering signal intensity of the coating at 13.9 GHz demonstrated a substantial reduction in signal intensity on the coated side compared with that on the PEC side [52], with the main lobe magnitude recorded at −7.9 dB·m^2. The simulation results demonstrate that SiZrBCN-16 ceramics exhibit excellent EMW absorption performance in practical applications.

3.3 Analysis of EMW attenuation mechanism

To further investigate the origin of the polarization characteristics of the SiZrBCN-16 ceramic, multiple structural models were constructed and optimized via DFT simulations on the basis of its multiphase composition of SiC/β-Si_3N_4/ZrC_xN_{1-x}/C [53]. In general, the electronic structure of a ceramic undergoes significant modifications under the influence of electronegativity differences between atoms, crystal surface states, internal defects, and grain boundary effects. Specifically, the electronegativity disparity drives the bonding electrons to migrate toward more electronegative atoms. Nonbonding lone pair electrons, such as those at crystal defects and grain boundaries, induce electron localization and the formation of localized positive and negative charge centers. This effect enables the material to exhibit a significant polarization response under an alternating electric field.

For example, in SiC and β-Si_3N_4, the partial density of states (PDOS) is predominantly contributed by the s and p orbitals of Si, C, and N atoms, as depicted in Fig. 7. The high degree of p-orbital overlap between Si and C atoms, as well as between Si and N atoms, leads to the formation of strong covalent bonds. The band gap values slightly vary depending on the computational methods and experimental conditions. The band gaps of SiC and β-Si_3N_4 are 1.37 and 3.12 eV, respectively, demonstrating their characteristic semiconductor behavior [54].

However, C and N atoms randomly occupy octahedral interstitial sites within the Zr sublattice, forming a ZrC_xN_{1-x} solid solution in the SiZrBCN ceramics. This homogeneous distribution of coexisting N and C atoms within the lattice significantly

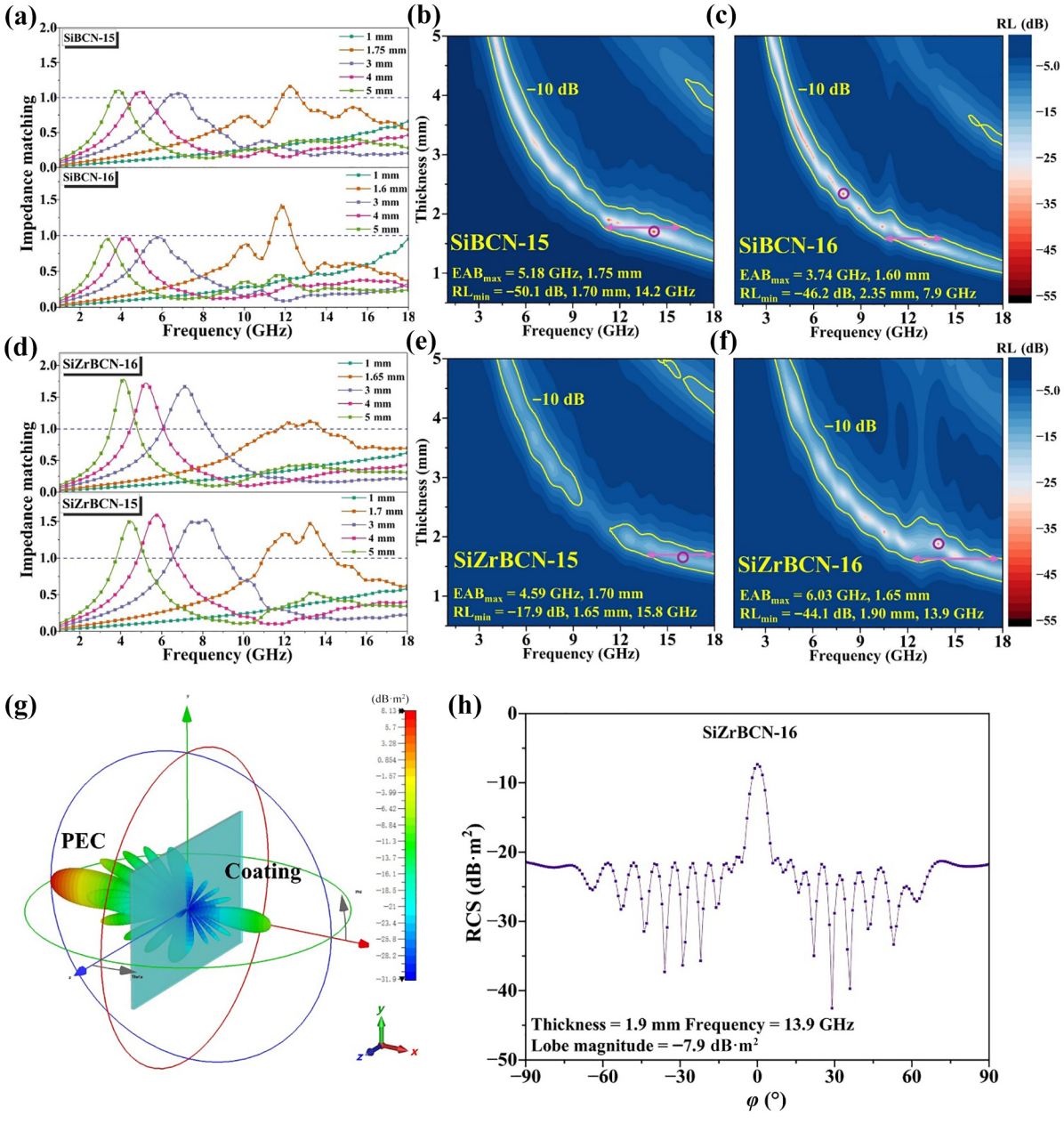

Fig. 6 Impedance matching and reflection loss diagram of (a–c) SiBCN and (d–f) SiZrBCN ceramics after annealing at 1500 °C (i.e., SiBCN-15 and SiZrBCN-15) and 1600 °C (i.e., SiBCN-16 and SiZrBCN-16), respectively. (g, h) RCS simulation and reflection curves of SiZrBCN-16.

reconstructs the electronic structure of ZrC_xN_{1-x}. Accordingly, structural models of ZrC were constructed, and the ZrC_xN_{1-x} structures were derived from the ZrC primitive lattice by substituting nitrogen atoms for carbon atoms. Given the multiple possible configurations of C and N atomic positions at each composition ratio, a 2×2×1 supercell of ZrC was generated to ensure a relatively uniform atomic distribution. Figure 8 presents the structurally optimized crystal models of ZrC, $ZrC_{14}N_2$, $ZrC_{12}N_4$, $ZrC_{10}N_6$, ZrC_8N_8, and ZrN.

Figure 9 presents the PDOS and electron density difference (EDD) slice maps on the (001) crystal plane for ZrC_xN_{1-x}. Compared with the crystal structures of ZrC and ZrN (Figs. 9(a) and 9(f)), the coexistence of C and N atoms significantly changes the electronic structure and bonding characteristics of the $ZrC_{10}N_6$ solid solution in Figs. 9(b) and 9(e). Within the ZrC_xN_{1-x} solid solution, electronegativity differences drive electron redistribution. Zr atoms exhibit enhanced positive charge depletion due to valence electron loss, whereas nitrogen atoms form highly localized negative charge accumulation regions through strong electron capture. Notably, electron density difference slices reveal pronounced electron transfer between Zr–C and Zr–N bonds, elucidating the underlying electron transfer mechanisms and structural interactions, providing insight into the complex electronic interactions in this system [55]. Specifically, the integration of the projected density of states for Zr 4d and C 2p in ZrC_xN_{1-x} reveals a pronounced decrease in charge accumulation. As the occupancy of nitrogen atoms within the unit cell increases, the contribution of N 2p orbitals to the total density of states progressively increases. This is reflected in the growing integrated area of the N 2p partial density of states. Simultaneously, the high electronegativity of nitrogen drives the preferential accumulation of valence electrons in N 2p orbitals. This shifts the bonding energy distribution toward ionic electrostatic interactions, suppressing the electron delocalization characteristic of covalent

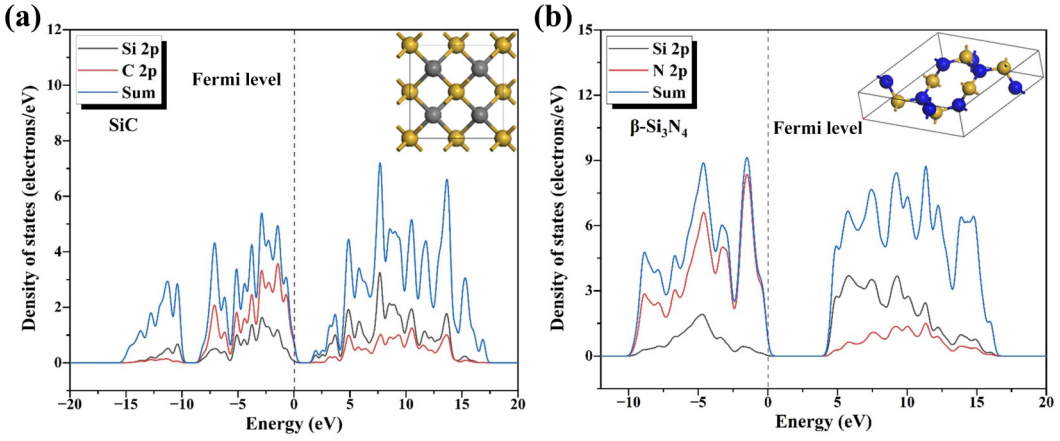

Fig. 7 Crystal structures and PDOS of SiC (denoting β-SiC) and β-Si_3N_4 ceramics.

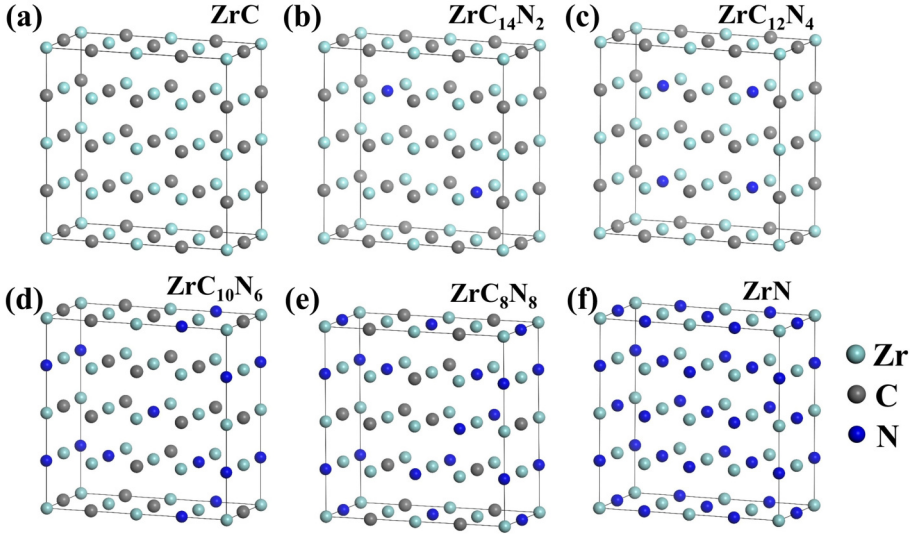

Fig. 8 Crystal models of ZrC, $ZrC_{14}N_2$, $ZrC_{12}N_4$, $ZrC_{10}N_6$, ZrC_8N_8, and ZrN.

bonding. Consequently, the free electron concentration decreases because electron localization is dominated by ionic bonding. Furthermore, the increased proportion of Zr–N bonds generates stronger electric dipoles (dipole moment $\mu = q \times d$, where q is the charge separation magnitude and d is the bond length of Zr–N) [56]. The random distribution of C and N atoms, with delocalized electrons surrounding Zr atoms, enhances electron localization and accelerates dipole reorientation [57].

Furthermore, nanoscale multiphase ceramics contain high-density interfacial structures that generate significant interface polarization under applied electric fields. This constitutes one of the primary mechanisms for electromagnetic wave energy absorption in such ceramics [58–60]. Within SiZrBCN-16 multiphase ceramics, distinct electronic structures exist between the constituent phases. For example, ZrC acts as a metallic conductor, whereas SiC and β-Si_3N_4 are semiconductors with different band gap values. Moreover, compared with bulk phases, crystal surfaces exhibit fundamentally different coordination environments, resulting in thermodynamically unstable states. The inherent high-energy states of surface unpaired electrons and contributions from high-energy localized surface states drive spontaneous energy minimization. During high-temperature grain growth in SiZrBCN ceramics, coherent or semicoherent interfaces form between dissimilar or identical grains. These interfaces relax through numerous defects or amorphous carbon layers, essentially reducing the interfacial energy spontaneously to achieve thermodynamic stability. This phenomenon is directly related to surface energy modulation mechanisms and fundamentally depends on the continuity of the atomic arrangement and electronic structure at the interfaces. Consequently, significant lattice distortion and electronic rearrangement occur during interface formation between nanoparticles. The construction of interface models can partially reveal the origin of interface polarization [61].

Given the inherent complexity of interface models requiring numerous atoms in structural files, we balanced computational accuracy with model simplification by constructing ZrC(001)/β-Si_3N_4(001) and ZrN(100)/SiC(110) interfaces, where the β-Si_3N_4(001) was transformed into a tetragonal lattice by redefining basis vectors while preserving atomic periodicity. Semicoherent grain boundaries were achieved through supercell construction on both crystalline phases (Fig. 10). To minimize initial stresses from lattice mismatch/geometric misalignment and achieve thermodynamically stable configurations, systematic structural optimization was performed via the CASTEP code, with iterative relaxation until convergence criteria were met.

The atoms at both sides of the interface are displaced due to lattice mismatch and chemical bond reconstruction during structural optimization. Elastic strain induced by lattice constant differences is subsequently released through bond length/angle adjustments or defect introduction. This distortion in the surface atomic layers of crystals on both sides of the interface (e.g., ZrC in

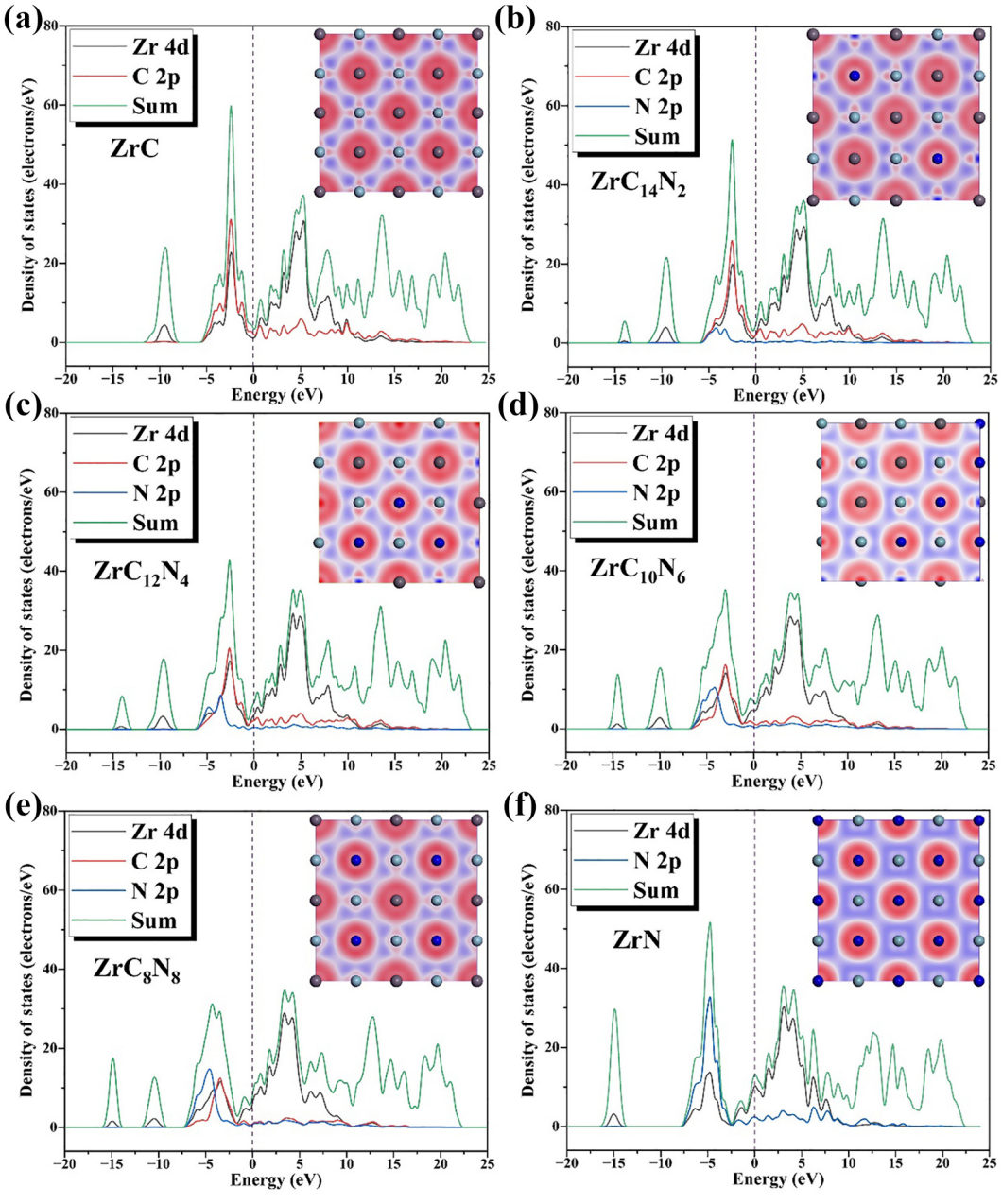

Fig. 9 PDOS and EDD slice maps of ZrC, $ZrC_{14}N_2$, $ZrC_{12}N_4$, $ZrC_{10}N_6$, ZrC_8N_8, and ZrN.

Fig. 10(b)) generates correlated effects through electronic rearrangement, manifested as modified orbital hybridization from altered interatomic distances, causing redistribution of DOS near the Fermi level [62]. Analysis on the basis of the electron density difference (Figs. 10(a)–10(g)) and projected density of states (Figs. 10(h) and 10(i)) reveals significant charge transfer at the interface. For the ZrC(001)/β-Si_3N_4(001) interface, significant electron rearrangement occurs between the interfacial Zr–N and Si–C atoms. This redistribution is triggered by changes in their coordination environments and electronegativity differences, as revealed by the PDOS analysis in Figs. 8(a), 8(b), 9(a), and 9(f). The 4d orbitals of the Zr atoms exhibit a directional shift toward the adjacent 2p orbitals of the N atoms (Fig. 10(h)). In the ZrN(100)/SiC(110) interface structure, we observed a shift of the Si 2p orbitals toward the N 2p orbitals (Fig. 10(i)). These newly formed energy levels at the interface increase the interfacial bonding strength and reduce the interfacial energy. Energy dissipation occurs during electron migration due to charge scattering, and this effect is amplified by the high charge density at incoherent interfaces [63]. Simultaneously, the interfacial charge reconstruction process forms additional dipole response centers [64]. When the dipole relaxation time matches the frequency of the electromagnetic wave, electromagnetic energy is converted into thermal energy due to damping during reorientation, a phenomenon known as Debye relaxation loss [65]. Therefore, the dipole groups formed at the numerous interfaces can cover a broad distribution of relaxation times [66,67].

Furthermore, under an applied electric field, the three-dimensional carbon network provides conduction pathways for electron transport. However, the presence of B and N atoms introduces defect sites that impede electron flow, thereby inducing conductive loss [68]. To investigate the influence of B and N atoms on the electronic structure of the carbon matrix, atomic models representing the C–B–C, C–N–C, and C–B–C–N–C configurations were constructed, and their charge density differences were calculated, as shown in Fig. 11. The electron

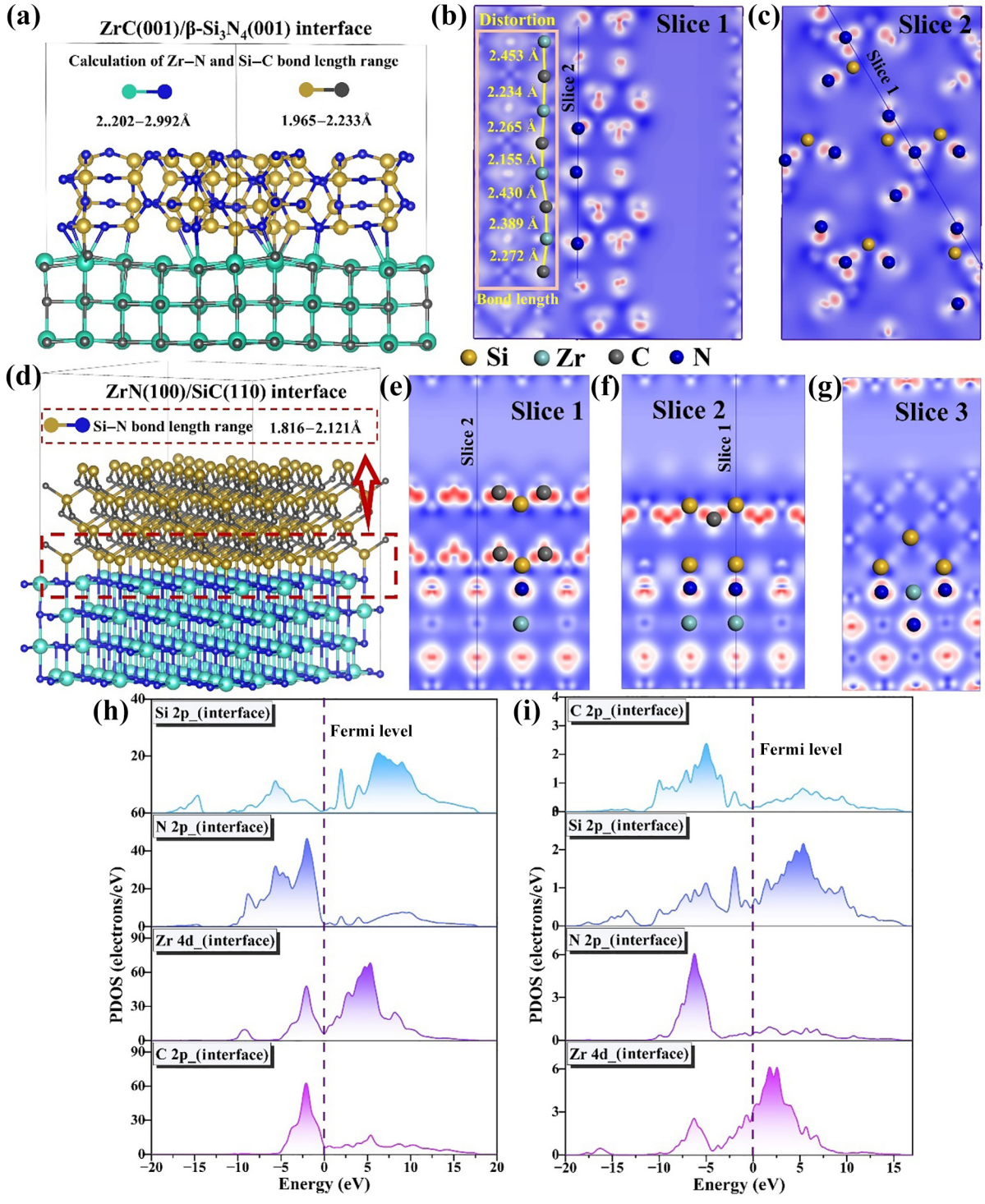

Fig. 10 (a–c) Interface models of ZrC(001)/β-Si_3N_4(001) and EDD slice maps at interfaces. (b–g) Interface models of ZrN(100)/SiC(110) and EDD slice maps at interfaces. (h, i) PDOS of atoms at interfaces of ZrC(001)/β-Si_3N_4(001) and ZrN(100)/SiC(110) after structural optimization.

density difference is visualized via cyan and yellow isosurfaces, which represent electron accumulation and depletion, respectively. A clear observation of localized charge transfer, which leads to the formation of electric polarization centers, effectively demonstrates the origin of the impediment to electron transport. Moreover, the generation of free electrons requires overcoming the binding energy from local atoms, a process for which the high-frequency electromagnetic field provides the necessary energy. Moreover, the multiscale architecture of the carbon network, which is dictated by the annealing temperature and grain size, generates a hierarchy of electron transport pathways and polarization features within the multiphase ceramic. Under an applied electromagnetic field, these features act in concert with the inherent multilevel interfaces to activate distinct relaxation processes. Collectively, these synergistic mechanisms underpin the pronounced dispersion of the dielectric parameters observed in most carbon-containing composite ceramics at high frequencies [12,69].

Building upon our previous analysis, we propose a microscopic electromagnetic loss mechanism for SiC/β-Si_3N_4/ZrC_xN_{1-x}/C ceramics. The response of ZrC_xN_{1-x} to electromagnetic waves

originates from charge separation induced by the difference in electronegativity between atoms. The formation of strong electric dipoles facilitates orientation polarization under an applied electric field. Furthermore, lattice distortion at the interfaces leads to a locally asymmetric distribution of charge. Within these semicoherent interfaces, electrons form new bonding configurations, giving rise to new energy levels. The migration and redistribution of electrons generate intrinsic electric dipole moments. Consequently, under an electromagnetic field, the synergistic effects of dipole reorientation polarization, space charge transfer, and conductive loss contribute to significant polarization relaxation loss, thereby inducing strong polarization loss and enabling efficient broadband electromagnetic wave absorption. Additionally, the electromagnetic wave absorption mechanisms for the SiBCN and SiZrBCN ceramics are summarized in Fig. 12.

4 Conclusions

In summary, the phase composition, microstructure, and electromagnetic wave absorption performance of the SiZrBCN and SiBCN ceramics were investigated after annealing at high annealing temperatures up to 1800 °C. Zr in SiBCN ceramics significantly influences the phase composition and transformation; it promotes the formation of a multiphase ceramic structure dominated by ZrC_xN_{1-x}, β-Si_3N_4, and SiC at 1600 °C (SiZrBCN-16), and this multiphase structure transforms into SiC/ZrB_2 at 1800 °C (SiZrBCN-18). In contrast, SiBCN-16 and SiBCN-18 only consist of the SiC phase. Under high-vacuum non-pressure annealing conditions, the introduction of Zr increases the stabilization temperature of the carbon network in SiBCN-based ceramics to 1600 °C. In addition, owing to the destruction of the B–C–N network structure at 1800 °C, the released B atoms diffuse into the ZrC_xN_{1-x} lattice, leading to the

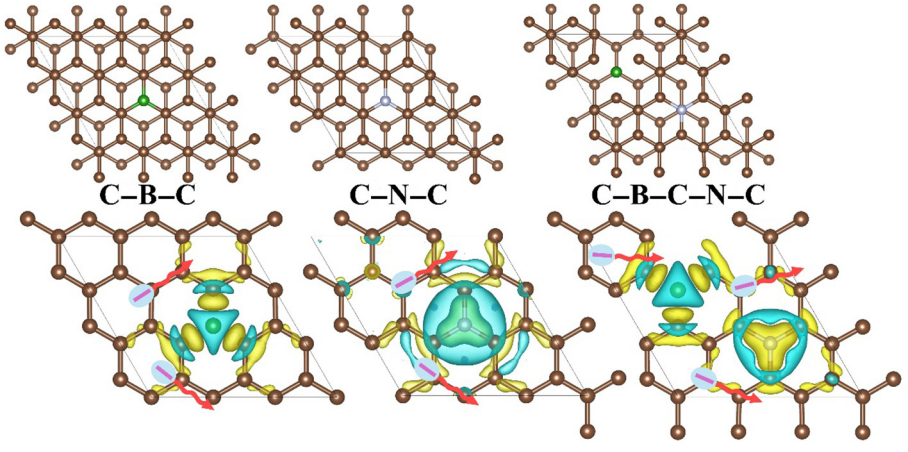

Fig. 11 Structure and charge density difference of C–B–C, C–N–C, and C–B–C–N–C.

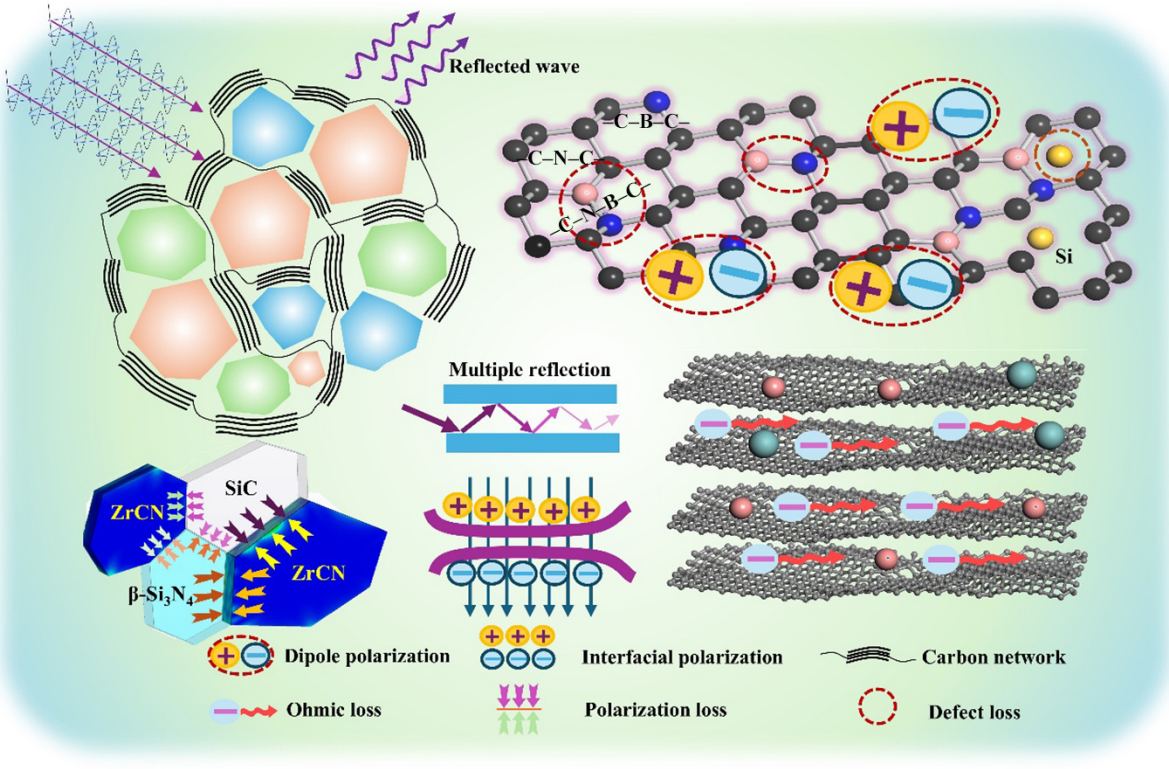

Fig. 12 Proposed electromagnetic wave attenuation mechanisms for SiBCN and SiZrBCN ceramics.

formation of ZrB_2. In addition, the electronegativity difference between C and N drives the formation of electric dipoles in ZrC_xN_{1-x}. Analysis of the electronic structures and charge transfer at the ZrC(001)/β-Si_3N_4(001) and ZrN(100)/SiC(110) interfaces elucidates the origin of interfacial charge transfer and polarization at the atomic scale. Specifically, the charge transfer at the interfaces originates from distortions caused by the semicoherent structure and the formation of new chemical bonds. The abundant dipoles, interfacial architectures, carbon networks, and defect-induced polarization centers in the SiZrBCN-16 ceramics synergistically increase polarization loss under electromagnetic wave irradiation. Significantly, the SiZrBCN-16 ceramic achieves a 6.03 GHz effective absorption bandwidth at a thickness of 1.65 mm, with a minimum reflection loss of −44.1 dB at 1.9 mm. This integrated computational–experimental approach provides a fundamental strategy for designing thermally stable EMW absorption materials with superior performance at reduced thicknesses.

Acknowledgements

The authors thank the National Natural Science Foundation of China (No. 52472082) and the National Natural Science Fund for Excellent Young Scholars (Overseas) for their financial support. Bo Feng thanks the Postdoctoral Fellowship Program of CPSF (No. GZB20230994) for financial support.

Availability of data and materials

The data that support the findings of this study are available from the corresponding author upon reasonable request.

Competing interests

The authors have no competing interests to declare that are relevant to the content of this article.

References

[1] Yu YX, Xu WL, Xu J, *et al.* Conductivity of SiCNO–BN composite ceramics and their application in wireless passive temperature sensor. *Ceram Int* 2021, **47**: 14490–14497.

[2] Chen QQ, Li DX, Yang ZH, *et al.* SiBCN–reduced graphene oxide (rGO) ceramic composites derived from single-source-precursor with enhanced and tunable microwave absorption performance. *Carbon* 2021, **179**: 180–189.

[3] Yan YF, Cheng ZY, Chen T, *et al.* Rational high-entropy doping strategy via modular *in situ*/post solvothermal doping integration for microwave absorption. *J Adv Ceram* 2025, **14**: 9221168.

[4] Niu ZB, Li DX, Jia DC, *et al.* Heterogeneous oxidation behavior and kinetic mechanisms of SiBCN ceramic with structure of MA–SiBCN coated by PDCs–SiBCN. *J Eur Ceram Soc* 2024, **44**: 1520–1533.

[5] Yu Z, Ma MW, Liu ZY, *et al.* Hyperbranched polyborosilazanes derived SiBCN ceramic for high-temperature wave-transparent performance. *J Mater Sci Technol* 2024, **196**: 162–170.

[6] Wang Y, Luo CJ, Wu YF, *et al.* High temperature stable, amorphous SiBCN microwave absorption ceramics with tunable carbon structures derived from divinylbenzene crosslinked hyperbranched polyborosilazane. *Carbon* 2023, **213**: 118189.

[7] Wang Q, Deng YM, Dai MY, *et al.* Multiphase ceramic SiBCN–ZrO_2 /ZrC/ZrB_2/SiC with ultra-wide bandwidth electromagnetic absorption. *Chem Eng J* 2024, **498**: 155392.

[8] Song CK, Liu XF, Ye F, *et al.* Mechanical and dielectric properties of SiC_f/BN/SiBCN composites via different synthesis technologies. *J Eur Ceram Soc* 2019, **39**: 4417–4423.

[9] Liu C, Guo X, Tong YC, *et al.* Vat photopolymerization 3D printing SiBCN ceramic metamaterials with strong electromagnetic wave absorption. *Addit Manuf* 2024, **87**: 104239.

[10] Yu ZJ, Chen T, Du HZ, *et al.* Single-source-precursor derived SiOC ceramics with *in-situ* formed CNTs and core–shell structured CoSi@C nanoparticles towards excellent electromagnetic wave absorption properties. *J Adv Ceram* 2023, **12**: 1119–1135.

[11] Ding Q, Zhan ZK, Zhang ZB, *et al.* Microstructure evolution and excellent electromagnetic wave absorption performance of SiBCN fibers. *Ceram Int* 2024, **50**: 39965–39974.

[12] Song Y, Liu ZY, Zhang XC, *et al.* Single source precursor derived SiBCNHf ceramic with enhanced high-temperature microwave absorption and antioxidation. *J Mater Sci Technol* 2022, **126**: 215–227.

[13] Zhang ZY, Yang JC, Lu L, *et al.* Electromagnetic wave absorbing performance of SiZrCN ceramic nanocomposites with tailored structure and composition. *J Cent South Univ* 2024, **55**: 2910–2924. (in Chinese)

[14] Wang J, Xin L, Zhang MW, *et al.* Structural evolution and dielectric properties of $(1-x)Sr_2SiO_4$–$xBa_{0.5}Sr_{0.5}TiO_3$ microwave dielectric ceramics. *Ceram Int* 2025, **51**: 43827–43835.

[15] Wen QB, Feng Y, Yu ZJ, *et al.* Microwave absorption of SiC/HfC_xN_{1-x}/C ceramic nanocomposites with HfC_xN_{1-x}–carbon core–shell particles. *J Am Ceram Soc* 2016, **99**: 2655–2663.

[16] Jiang JP, Yan LW, Li JT, *et al.* Lightweight, thermally insulating SiBCN/Al_2O_3 ceramic aerogel with enhanced high-temperature resistance and electromagnetic wave absorption performance. *Chem Eng J* 2024, **501**: 157656.

[17] Yang Q, Chen PG, Li XC, *et al.* Rational design of SiBCN ceramics with excellent attenuation to strong electromagnetic-wave-absorbing properties at low frequency. *Compos Part B—Eng* 2024, **280**: 111486.

[18] Zhao MX, Liu YS, Chai N, *et al.* Effect of SiBCN content on the dielectric and EMW absorbing properties of SiBCN–Si_3N_4 composite ceramics. *J Eur Ceram Soc* 2018, **38**: 1334–1340.

[19] Zhang WZ, He XL, Du Y. EMW absorption properties of *in situ* growth seamless SiBCN–graphene hybrid material. *Ceram Int* 2019, **45**: 659–664.

[20] Luo CJ, Miao P, Tang YS, *et al.* Excellent electromagnetic wave absorption of MOF/SiBCN nanomaterials at high temperature. *Chinese J Aeronaut* 2021, **34**: 277–291.

[21] Zhang KL, Wang Z, Yan YF, *et al.* Dielectric–magnetic manipulation of reduced graphene oxide permittivity for enhanced electromagnetic wave absorption. *J Adv Ceram* 2024, **13**: 1974–1984.

[22] Erdem Ü, Sarı KA, Dogan D, *et al.* Fabrication and characterization of ferromagnetic FeMnCo/nanofibers for broadband electromagnetic wave absorption. *J Alloy Compd* 2025, **1036**: 181958.

[23] Zhang SJ, Lan D, Zheng JJ, *et al.* Insights into polarization relaxation of electromagnetic wave absorption. *Cell Rep Phys Sci* 2024, **5**: 102206.

[24] Cui ZR, Yang ML, Han GY, *et al.* Recent advances in carbon composite films for high-performance, multifunctional and intelligent electromagnetic interference shielding and electromagnetic wave absorption. *Carbon* 2024, **230**: 119627.

[25] Duan YP, Li MQ, Guo Y, *et al.* Improving electromagnetic wave absorption performance by adjusting the proportion of brittle BCC phase in $FeCoNiCr_{0.4}Mn_x$ high-entropy alloys. *Mater Today Phys* 2024, **49**: 101596.

[26] Sengwa RJ, Charan CP. Radio frequencies dielectric and electrical properties of nanomaterial-in-polymer-in-nanomaterial based PMMA/OMMT composites. *Mater Lett* 2025, **400**: 139157.

[27] Zayoud W, El Kamel F, Jorel C, *et al.* Dielectric properties of the ZrO_2/$SrTiO_3$ heterostructures. *J Alloy Compd* 2025, **1036**: 181965.

[28] Li Q, Zhang JH, Wang ZC, *et al.* Influence of microstructure evolution on temperature-dependent dielectric and electromagnetic wave absorption properties of PDCs–SiC. *Ceram Int* 2022, **48**: 8596–8604.

[29] Wang JS, Wang LY, Zhu YB, *et al.* Microwave absorption properties of PDCs–SiC(N) based on heat treatment at different temperatures. *Ceram Int* 2024, **50**: 40666–40677.

[30] Li N, Zong Z, Zhang F, *et al.* Barium ferrite with high anisotropy for ultra-broadband microwave absorption. *Adv Funct Mater* 2025, **35**: 2414694.

[31] Zhao B, Yan ZK, Du YQ, *et al.* High-entropy enhanced microwave attenuation in titanate perovskites. *Adv Mater* 2023, **35**: 2210243.
[32] Zhang WM, Dai FZ, Xiang HM, *et al.* Enabling highly efficient and broadband electromagnetic wave absorption by tuning impedance match in high-entropy transition metal diborides (HE TMB_2). *J Adv Ceram* 2021, **10**: 1299–1316.
[33] Li YJ, Liu SR, Zhai HL, *et al.* The influence of different vacancies on Zr(0001)/SiC close-packed interface performance: A first-principles study. *J Nucl Mater* 2025, **603**: 155461.
[34] Guo HL, Zhang ZF, Guo YZ, *et al.* Impact of the interface vacancy on Schottky barrier height for Au/AlN polar interfaces. *Appl Surf Sci* 2020, **505**: 144650.
[35] Chen ZB, Yao BQ, Yin DL, *et al.* Wetting behavior of AgCu–Ti filler metal on SiC ceramics surface pre-treated by ion bombardment. *Ceram Int* 2020, **46**: 9065–9069.
[36] Ye F, Zhang LT, Yin XW, *et al.* Dielectric and EMW absorbing properties of PDCs–SiBCN annealed at different temperatures. *J Eur Ceram Soc* 2013, **33**: 1469–1477.
[37] Chen S, Wan LY, Xie D, *et al.* Adducing crystalline features from Raman scattering studies of cubic SiC using different excitation wavelengths. *J Phys D Appl Phys* 2017, **50**: 115102.
[38] Wen QB, Yu ZJ, Riedel R. The fate and role of *in situ* formed carbon in polymer-derived ceramics. *Prog Mater Sci* 2020, **109**: 100623.
[39] Feng B, Peter J, Fasel C, *et al.* High-temperature phase and microstructure evolution of polymer-derived SiZrCN and SiZrBCN ceramic nanocomposites. *J Am Ceram Soc* 2020, **103**: 7001–7013.
[40] Niu ZB, Li DX, Jia DC, *et al.* Heterogeneous oxidation of different atomic clusters in amorphous SiBCN ceramic associated with phase separation. *Corros Sci* 2024, **227**: 111723.
[41] Liu ZY, Zhao HY, Tian YS, *et al.* Synthesis and ceramization of a soluble single-source precursor for SiZrBCN multinary ceramics with enhanced oxidation resistance. *J Alloy Compd* 2025, **1035**: 181177.
[42] Xue JM, Tang ZM, Wang CX, *et al.* Microstructure and EMW absorption properties of PDCs-SiCN(Ti) ceramics with adjustable SiC nanowires and TiC nanocrystallines. *Mater Res Bull* 2024, **176**: 112804.
[43] Tong YC, Guo X, Liu C, *et al.* Shellular SiCN ceramics with integrated structure and function realizing full electromagnetic wave absorption in the X-band. *J Eur Ceram Soc* 2024, **44**: 5055–5067.
[44] Wen QB, Yu ZJ, Riedel R, *et al.* Single-source-precursor synthesis and high-temperature evolution of a boron-containing SiC/HfC ceramic nano/micro composite. *J Eur Ceram Soc* 2021, **41**: 3002–3012.
[45] Elmahaishi MF, Azis RS, Ismail I, *et al.* Influence of particle size on the magnetic and microwave absorption properties of magnetite via mechano-mechanical methods for micro-nano-spheres. *Nano-Struct Nano-Objects* 2024, **39**: 101207.
[46] Liao WH, Huang K, Xu WW, *et al.* Broadband microwave absorption and electromagnetic properties of Gd–Al–Co-doped M-type barium hexaferrite in 2–18 GHz range. *J Magn Magn Mater* 2024, **612**: 172609.
[47] Lv HL, Yang ZH, Liu B, *et al.* A flexible electromagnetic wave-electricity harvester. *Nat Commun* 2021, **12**: 834.
[48] Ye FX, Guo XJ, Chen YC, *et al.* Effect of Ce doping on the structure and wave absorption properties of barium ferrite. *Ceram Int* 2025, **51**: 15890–15901.
[49] Shu RW, Zhang GY, Wang X, *et al.* Fabrication of 3D net-like MWCNTs/$ZnFe_2O_4$ hybrid composites as high-performance electromagnetic wave absorbers. *Chem Eng J* 2018, **337**: 242–255.
[50] Wang L, Huang MQ, Yu XF, *et al.* Engineering polarization surface of hierarchical ZnO microspheres via spray-annealing strategy for wide-frequency electromagnetic wave absorption. *J Mater Sci Technol* 2022, **131**: 231–239.
[51] Wang WC, Wang LY, Huang J, *et al.* Multi-heterointerface lightweight ceramics achieving temperature-insensitive dielectric properties for high-temperature electromagnetic wave effective absorption. *J Adv Ceram* 2025, **14**: 9221135.
[52] Chen YQ, Chen M, Lei HY, *et al.* Microwave-assisted synthesis of high-performance TaC nanorods for enhanced electromagnetic wave absorption. *J Adv Ceram* 2025, **14**: 9221130.
[53] Tozini D, Forti M, Gargano P, *et al.* Charge difference calculation in Fe/Fe_3O_4 interfaces from DFT results. *Proc Mat Sci* 2015, **9**: 612–618.
[54] Zhang XD, Quan SY, Ying CH, *et al.* Theoretical investigations on the structural, lattice dynamical and thermodynamic properties of XC (X = Si, Ge, Sn). *Solid State Commun* 2011, **151**: 1545–1549.
[55] Wen JM, Chen G, Hui SC, *et al.* Plasma induced dynamic coupling of microscopic factors to collaboratively promote EM losses coupling of transition metal dichalcogenide absorbers. *Adv Powder Mater* 2024, **3**: 100180.
[56] Pan YY. Insights of the pH-dependent emission of carbon dots: A density functional theory study. *J Phys Conf Ser* 2023, **2587**: 012045.
[57] Lv HL, Yao YX, Li SC, *et al.* Staggered circular nanoporous graphene converts electromagnetic waves into electricity. *Nat Commun* 2023, **14**: 1982.
[58] Xiao JX, Zhan BB, He MK, *et al.* Interfacial polarization loss improvement induced by the hollow engineering of necklace-like PAN/carbon nanofibers for boosted microwave absorption. *Adv Funct Mater* 2025, **35**: 2316722.
[59] Zhang HB, Cheng JY, Wang HH, *et al.* Initiating VB-group laminated NbS_2 electromagnetic wave absorber toward superior absorption bandwidth as large as 6.48 GHz through phase engineering modulation. *Adv Funct Mater* 2022, **32**: 2108194.
[60] Wang ZJ, Zhang F, Wang NN, *et al.* Ternary layered boride MoAlB: A novel thermo-regulation microwave absorbing ceramic material. *J Adv Ceram* 2024, **13**: 699–710.
[61] Wang WZ, Liu R, Tao JQ, *et al.* Enhancing dipole polarization loss in conjugated metal-organic frameworks via coordination symmetry breaking under electromagnetic field. *Adv Powder Mater* 2025, **4**: 100302.
[62] Zhou YK, Tang CH, Li SY, *et al.* Quantifying heterogeneous interface effect of Fe_3O_4(111)/C for enhanced low-frequency electromagnetic wave absorption. *Carbon* 2025, **232**: 119792.
[63] Yan MY, Pan YL, He P, *et al.* Mechanically strong SiC aerogels with broadband electromagnetic wave absorption enabled by hollow skeleton and interface engineering. *Chem Eng J* 2024, **497**: 154556.
[64] Zeng XJ, Jiang X, Ning Y, *et al.* Construction of dual heterogeneous interface between zigzag-like Mo–MXene nanofibers and small CoNi@NC nanoparticles for electromagnetic wave absorption. *J Adv Ceram* 2023, **12**: 1562–1576.
[65] Qin M, Zhang LM, Zhao XR, *et al.* Defect induced polarization loss in multi-shelled spinel hollow spheres for electromagnetic wave absorption application. *Adv Sci* 2021, **8**: 2004640.
[66] Zhu H, Weng XL, Liao M, *et al.* ZrO_2-interface-engineered SiC nanofiber aerogel with integrated hydrophobicity, thermal insulation, and broadband electromagnetic wave absorption. *Appl Surf Sci* 2025, **711**: 164079.
[67] Liang J, Zhu SY, Chen DW, *et al.* Dual built-in electric field engineering in heterostructure nickel–cobalt bimetallic composites for boosted electromagnetic energy dissipation. *Adv Powder Mater* 2025, **4**: 100344.
[68] Lv HL, Yang ZH, Wang PL, *et al.* A voltage-boosting strategy enabling a low-frequency, flexible electromagnetic wave absorption device. *Adv Mater* 2018, **30**: 1706343.
[69] Liang J, Ye F, Cao YC, *et al.* Defect-engineered graphene/Si_3N_4 multilayer alternating core–shell nanowire membrane: A plainified hybrid for broadband electromagnetic wave absorption. *Adv Funct Mater* 2022, **32**: 2200141.